

Fluorescence diffuse optical tomography for free-space and multifluorophore studies

Anne Koenig
Lionel Hervé
Georges Gonon
CEA-LETI, Minatec
17 Rue des Martyrs
Grenoble Cedex 9, 38054
France

Véronique Josserand
Institut Albert Bonniot
INSERM U823
La Tronche Cedex 9, 38706
France

Michel Berger
Jean-Marc Dinten
Jérôme Boutet
Philippe Peltié
CEA-LETI, Minatec
17 Rue des Martyrs
Grenoble Cedex 9, 38054
France

Jean-Luc Coll
Institut Albert Bonniot
INSERM U823
La Tronche Cedex 9, 38706
France

Philippe Rizo
CEA-LETI, Minatec
17 Rue des Martyrs
Grenoble Cedex 9, 38054
France

1 Introduction

Near-infrared (NIR) fluorescence-enhanced diffuse optical tomography (fDOT) is an emerging cost-effective imaging modality for small animal imaging.^{1,2} It allows obtaining quantitative functional measurements and enables the three-dimensional (3-D) localization of the fluorescent targeted areas. However, in such systems, animal manipulation is a crucial point. It has to be efficient, not constraining, and safe for the animal.³

A continuous-wave (cw) fDOT system has been developed in our laboratory;⁴ similar instruments exist on the market.^{3,5,6} Originally designed for an animal restrained between two glass plates, our system has been extended for free-space or plate-free experiments. The original system equipment has been improved in two key areas: through the addition of a

Abstract. We present two major advances in preclinical fluorescence-enhanced diffuse optical tomography (fDOT) system and assess its performance. It is now possible to perform experiments without adaptation liquid or a glass plate over the animal, and our system is equipped with a filter wheel in order to discriminate two injected fluorophores. Evaluation carried out on characterization phantoms and *in vivo* on mice demonstrates enriched use of the system for biological studies on small animals. © 2010 Society of Photo-Optical Instrumentation Engineers. [DOI: 10.1117/1.3309738]

Keywords: optical tomography; medical imaging; image reconstruction; propagation; fluorescence.

Paper 08455RR received Dec. 23, 2008; revised manuscript received Dec. 4, 2009; accepted for publication Dec. 4, 2009; published online Mar. 1, 2010.

filter wheel and an extra planar laser associated to a triangulation method (Fig. 1). Thanks to the planar laser, which enables the acquisition of the animal's surface, the system now allows noncontact measurements and no longer requires immersing the animal or restraining it between plates.

A dedicated reconstruction scheme has been developed. A light propagation model, taking into account optical heterogeneities and boundary effects, is built up using the transmitted excitation light measurements and the description of acquisition geometry. The fluorescence yield is then reconstructed from the fluorescence light measurements using an algebraic reconstruction technique (ART) algorithm.⁷

In this paper, we point out the evolution of the experimental setup of our system, the associated reconstruction method, and their extension to free-space experiments. We then present experimental results obtained on heterogeneous phantoms that characterize our system. A Later section details a

Address all correspondence to: Anne Koenig, CEA-LETI, Minatec, 17 Rue des Martyrs, Grenoble Cedex 9, 38054, France. Tel: 33-4-38-78-37-30; Fax: 33-4-38-78-59-30; E-mail: anne.koenig@cea.fr

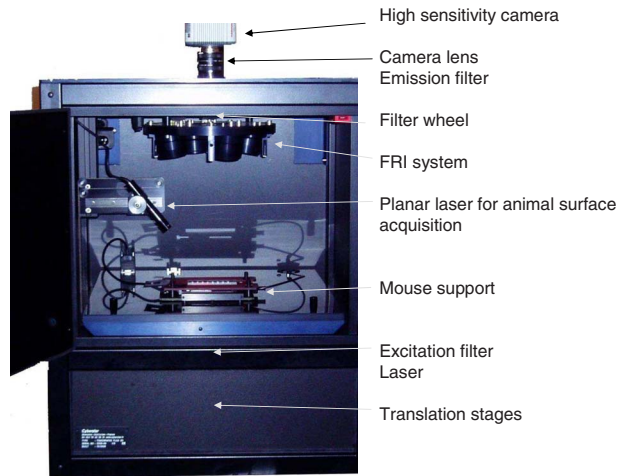


Fig. 1 Experimental setup. The tomograph is composed of a cooled CCD camera and a laser source coupled to translation stages. The system is also equipped with a filter wheel and an extra planar laser, giving access to the animal surface.

study on Swiss nude mice to validate our system's use for *in vivo* experiments.

2 Tomography Improvements

The tomograph was developed in collaboration with the Cyberstar Company on the basis of the experimental setup described in Ref. 4. It consists (Fig. 1) of a laser source (690 nm, 26 mW, Powertechnology) coupled to two motorized translation stages (THK) and a cooled 12-bit CCD camera (Orca EG, Hamamatsu). The laser excitation source describes a regular 2-mm-spaced grid under the animal support. For each source position, the CCD camera is focused at the median thickness of the animal and records first the transmitted (excitation) images and then the fluorescence (emission) filtered images.

In this study, the system has been updated in order to acquire small animal measurements in free-space experiments. The animal's surface is measured by a triangulation method involving an extra oblique planar laser. This surface is taken into account in the forward light propagation model by using "extrapolated boundary conditions."⁸ It consists in slightly increasing the size of the medium by a distance that depends on the refraction indexes and the diffusion coefficient and by imposing a null for the density wave at the new border.

2.1 Object Surface Acquisition

The tomograph is equipped with an extra oblique green planar laser connected with the x translation stage (Fig. 2). A green laser has been chosen because the absorption of its light is very strong and the maximum intensity distribution remains localized near the incidence point of the mouse skin. The more critical point is the roughness of the sample surface to avoid any laser reflexion. Other techniques exist in order to scan the object surface. For example, in quality control of mechanical pieces, galvanometers can be used. Our solution by triangulation method is simplest to use and is cost effec-

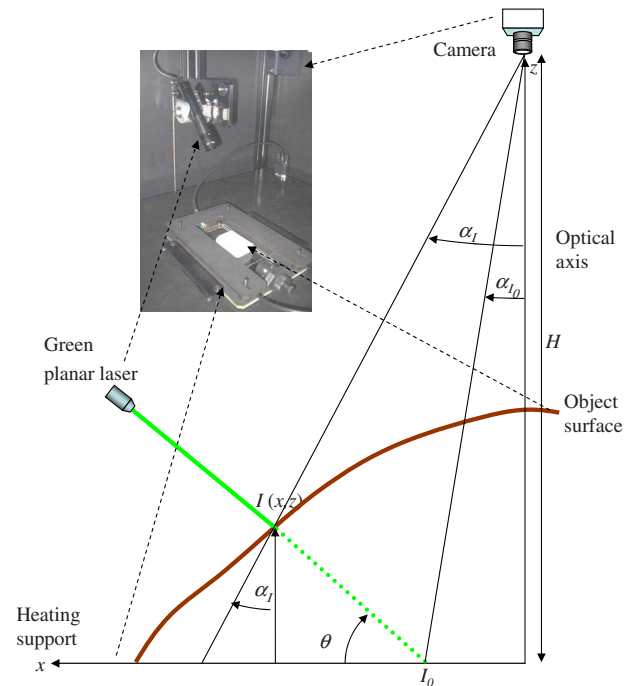


Fig. 2 Schema of the surface computation within the planar laser acquisition xz plane.

tive. In Ref. 9, Schulz et al. present a system that retrieves the 3-D surface information of the diffuse medium using a camera.

At a given x position, the intersection curve between the laser plane and the studied object is acquired by the top camera. The intersection is linearly distorted along the x axis depending on the height of the intersection. By using the triangulation formula and provided that no region is in the shadow of the planar laser, we recover the object surface with a laser scan.

We can demonstrate the validity of this method by using a calibrated phantom. This consists of a staircase black phantom with calibrated steps of 5-mm thickness each [Fig. 3(a)]. The computed surface is presented in Fig. 3(b), superimposed in red over the black-and-white image of the phantom. The different slices of this surface show that each step is recovered with the right thickness, as shown in the projection given in Fig. 3(c). As the laser makes a 45 deg angle with the vertical, the theoretical accuracy that can be reached is given by the equivalent CCD pixel size in the object plane—i.e., 200 times $\sqrt{2}$ μm . The error measured on the calibrated phantom is 300 μm , which is in accordance with the theoretical error.

After a smoothing step, these errors of the surface acquisition are taken into account by the computation of the attenuation map and its use during the reconstruction process.⁷ They remain at a level sufficient for reconstruction in good conditions.

2.2 Reconstruction Method

Here, the propagation of light modeled as a scalar field $\phi(\mathbf{r})$ in highly diffusive media is assumed to follow the Helmholtz equation:

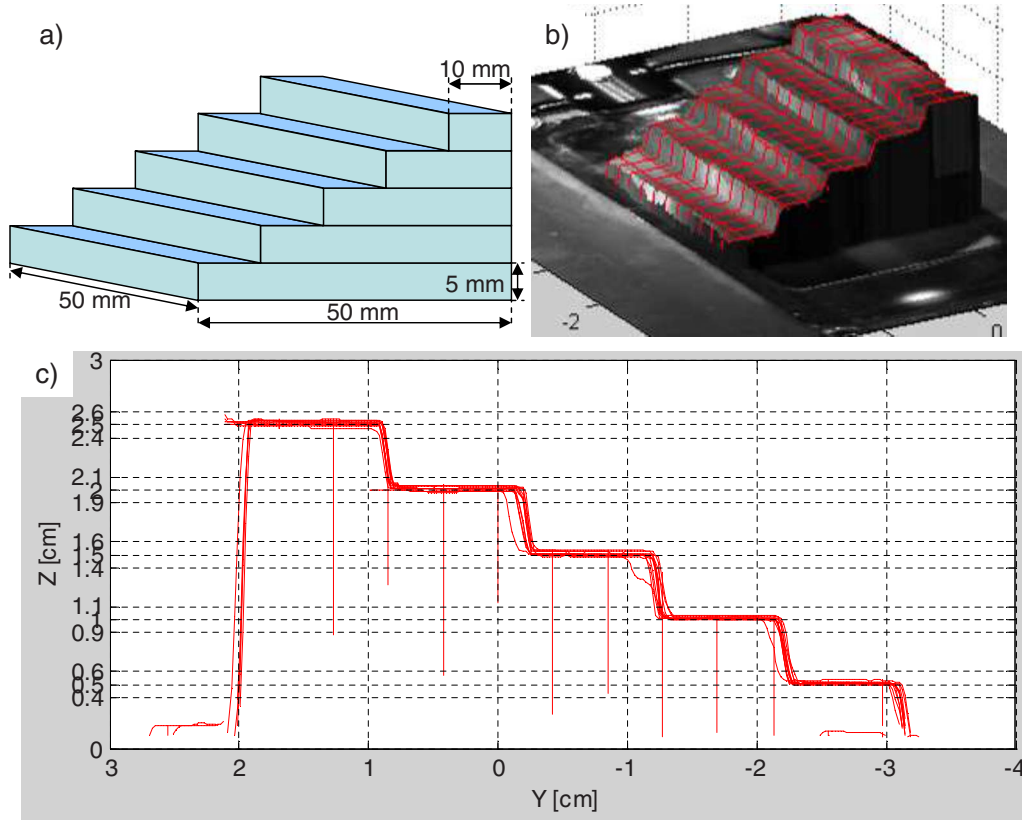


Fig. 3 Staircase phantom used to validate the surface acquisition: (a) schema of the phantom, (b) calculated surface superimposed onto the phantom photograph, and (c) transversal slice of the reconstructed staircase. (Color online only.)

$$\nabla^2 \phi_s(\mathbf{r}) - k(\mathbf{r})\phi_s(\mathbf{r}) = -\gamma \cdot \delta(\mathbf{r} - \mathbf{r}_s) \quad \text{with } k(\mathbf{r}) = 3\mu_a \cdot \mu'_s, \quad (1)$$

where \mathbf{r} is the position in the studied medium, index s is related to the source position, and δ is the Dirac function. $k(\mathbf{r})$ is a scalar map we call the “attenuation map,” which compounds the absorption and reduced scattering coefficients, and can also take into account effects of diffusion variations.⁷ The proportionality coefficient γ is related to the laser source intensity and the detection efficiency and has to be calibrated on a reference experiment using the phantom described in the following.

Using the animal surface provided by the planar laser, we can complete the equation system with the “extrapolated boundary conditions.”⁸ The discrete form of Eq. (1) is obtained by using a finite volume method applied on an unstructured mesh that conforms to the extrapolated boundary.¹⁰

Given a k map, we can compute the propagation function $G(\mathbf{r}_1, \mathbf{r}_2)$ of light in the medium between any points \mathbf{r}_1 and \mathbf{r}_2 :

$$(\nabla^2 - k)G(\mathbf{r}_1, \mathbf{r}_2) = -\delta(\mathbf{r}_1 - \mathbf{r}_2). \quad (2)$$

By modeling the laser source \mathbf{s} as a Dirac delta function position at \mathbf{r}_s , Eqs. (1) and (2) give the excitation density wave at any point \mathbf{r} of the medium:

$$\Phi^{ex}(\mathbf{r}_s, \mathbf{r}) = \gamma G(\mathbf{r}_s, \mathbf{r}) \quad (3)$$

The reconstruction process is then performed in two main steps, as shown in Fig. 4.

We first compute the attenuation $k(r)$ map by comparison of the Green’s functions G_{sd} to the excitation measurements U_{sd}^{exc} . This first step is itself an iterative process initialized with a homogeneous map $k_0(r)$.

Once this first step is completed, we end up with Green’s functions giving a valid description of the propagation of the light in the studied medium. The fluorescence yield can then be reconstructed from fluorescent measurements by using a classic iterative ART algorithm.¹¹ Convergence of the algorithm is achieved within 15 iterations and a relaxation parameter of 0.1.

The system is not strictly speaking underdetermined; however, it is very ill-conditioned. The regularization is obtained by stopping the iterations. The *ad hoc* ART iteration number has been estimated on several mice experiments.

2.3 Filtering

A filter wheel has been added to the system. This is useful for performing multiple functional analyses on the same animal and at the same time providing the use of different fluorophores. It has already been demonstrated in single-photon emission computed tomography (SPECT) that the use of sev-

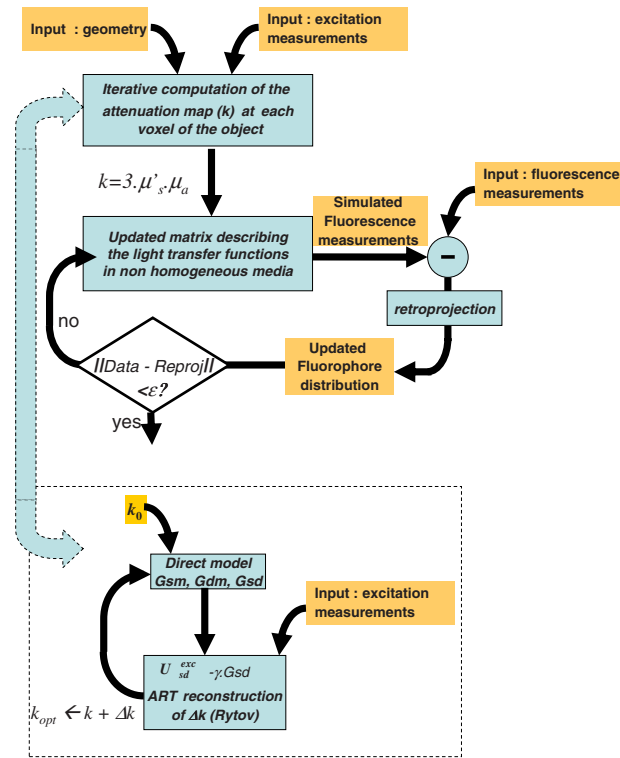


Fig. 4 Block diagram of the reconstruction algorithm. The reconstruction process is performed in two main steps: attenuation map computation detailed in the bottom dashed box, and iterative fluorescence quantity reconstruction.

eral markers can improve diagnostics.¹² For example, in optical imaging techniques, it is used to enable specific diagnosis of tumors¹³ or to validate the model of ovarian cancer used as presented in Ref. 14.

The excitation laser source wavelength is 690 nm. At present, two main fluorophores are used: Alexa 680 and Alexa 750 (Alexa Fluor Dye Series, Molecular Probes—Invitrogen). A bandpass 730AF30 filter (30-nm bandpass centered at 730 nm) makes it possible to see only Alexa 680, and a long-pass 770ALP filter (cut on at 770 nm) makes it possible to record both fluorophores' emission. The filters cut-on are chosen so that the filter response curve of the bandpass filter overlaps the emission curve of Alexa 680 and cuts at the very beginning of emission of Alexa 750 and so that the response curve of the long-pass filter overlaps a large part of the emission curve of Alexa 750 and cuts at the end of the emission curve of Alexa 680. The long-pass filter is separated enough from the excitation wavelength to correctly reject it and allows using any fluorophore with a fluorescence above 770 nm. Therefore, it is suitable for numerous configurations. The second (bandpass) filter was chosen to allow the demultiplexing of Alexa 750 and Alexa 680 spectra.

We measure experimentally on fluorescence reflectance imaging (FRI) images of capillary tubes containing the same quantity of fluorophore such that for Alexa 680, the ratio of the two filter's response (bandpass filter/long-pass filter) is 3.3, and for Alexa 750, the ratio of the two filters' response (long-pass filter/bandpass filter) is 20. These ratios indicate that Alexa 750 can be seen only by the long-pass filter and

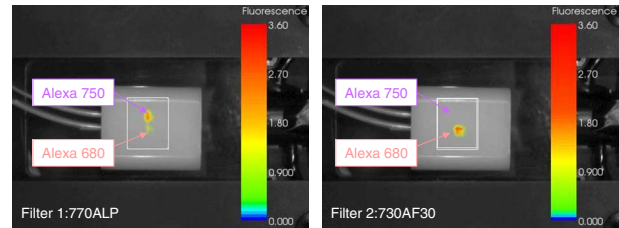
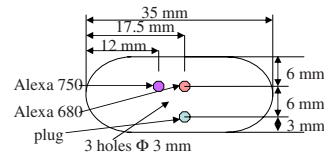


Fig. 5 Use of the filter wheel to separate two fluorophores: Alexa 680 and Alexa 750. Top: Schema of the phantom used. Bottom left: Reconstruction result with use of the high-pass filter; the two fluorophores are reconstructed, with a greater intensity for Alexa 750. Bottom right: Reconstruction result with use of the bandpass filter; only Alexa 680 is reconstructed.

that Alexa 680 can be seen by the two filters with, however, a lower value for the long-pass filter. The FRI system [2-D illumination by a crown of LEDs on the animal's region of interest (ROI) and records of light backscattered by the fluorescent markers on a CCD camera through a focusing lens] we used has been fully described in Ref. 15.

3 Tests and Results

The new functionalities of the tomograph have been tested on phantoms and mice.

3.1 Phantom Description

The phantom described in Fig. 5 (top) is used to test the separation of the two fluorophores according to the filter in use. Its bulk material is composed of a mixture of epoxy resin, titanium dioxide (TiO_2) powder for dispersers, and black ink as the absorber ($\mu_a = 0.2 \text{ cm}^{-1}$, $\mu'_s = 10 \text{ cm}^{-1}$)—the absorption coefficient was measured using an absorption spectrometer during the phantom making before adding TiO_2 powder. The diffusion coefficient is obtained after phantom making by fitting a transmitted optical signal through the phantom and through a range of known phantoms.

It is roughly a parallelepiped, 35 mm wide, 42 mm long, and 15 mm high. Capillary tubes are placed in two of the three 3-mm holes that are drilled in the phantom. They are separated by 2.5 mm. One of them contains Alexa 750, the other Alexa 680. The two solutions have been characterized to contain approximately 3 pmol of fluorophore. (They are prepared by diluted 3 pmol of fluorophore in a solution of Intralipid.) We use the two upper holes; the third one was used for other experiments intended to study separation in the z direction.

Another test phantom is delivered with the tomograph and enables the evaluation of the machine's stability. It has the same bulk material and the same dimensions as the phantom of Fig. 5, i.e., roughly a parallelepiped, 35 mm wide, 42 mm long, and 15 mm high. A fluorescent cylindrical inclusion (length 7 mm, diameter 2 mm; fluorescent glass fragment), equivalent to a concentration of $15 \mu\text{mol L}^{-1}$ Alexa 700, is

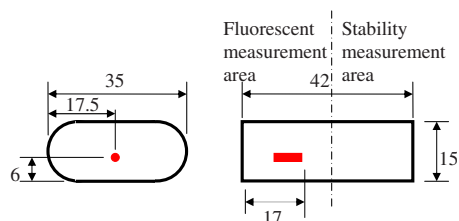


Fig. 6 Phantom used to test the repeatability and stability of the tomograph. The left part contains a fluorescent inclusion. The right part is homogeneous and is used to measure the γ parameter of Eq. (1).

positioned in a part of the phantom (see Fig. 6). The other part is homogeneous and is used to measure the γ parameter of Eq. (1); this enables evaluating the laser stability. The technique used to validate the phantom optical properties ($\mu a = 0.2 \text{ cm}^{-1}$, $\mu' s = 10 \text{ cm}^{-1}$) is the same as described earlier.

3.2 Filtering Test

Figure 5 (bottom left) shows that, using the long-pass filter, the two fluorophores are reconstructed but with a higher contrast for Alexa 750. On the right, using the bandpass filter, only Alexa 680 is reconstructed. The two reconstructions are presented in the same colormap.

We choose here to keep the long-pass filter that equipped our system in its first version in order to be able to compare our measurements to older ones done in this first configuration.

3.3 Repeatability

Several experiments have been performed over the fluorescent part of this phantom: five with the high-pass 770ALP filter (cut-off at 770 nm) and six with the bandpass 730AF30 filter (30-nm band-cut centered at 730 nm). The experiments are performed the same day for each filter (one day for the band-pass filter, and one day two weeks later for the high-pass filter). The system was turned on and off two times each day. In routine use of the tomograph, one experiment is done at least once per month over the fluorescent part of the phantom, and each day over the homogeneous part.

A curve showing the values of the γ parameter of Eq. (1) obtained on this homogeneous part is shown in Fig. 7 (top). The period covers 5 months of tomograph use and shows a good stability of the laser.

Figure 7 (bottom) presents the reconstructed fluorescence values measured in the overall reconstructed volume for each experiment. For these experiments, the excitation sources describe a regular 7 by 7.2 mm-spaced grid (1.4 cm \times 1.4 cm) under the phantom. The reconstructed volume is 9 by 9 by 16 voxels. The voxel size is 2 mm by 2 mm by 1 mm.

The observed 10% drift is due to photo-bleaching of the glass inclusion. This has been studied as described in Ref. 16.

3.4 In Vivo Mice Experiments Protocol

The global animal measurement protocol used is as follows: The animal is positioned on a heating holder free of upper glass plate or adaptation liquid. It can be gently maintained by the legs to reduce its movements. At first, the planar laser

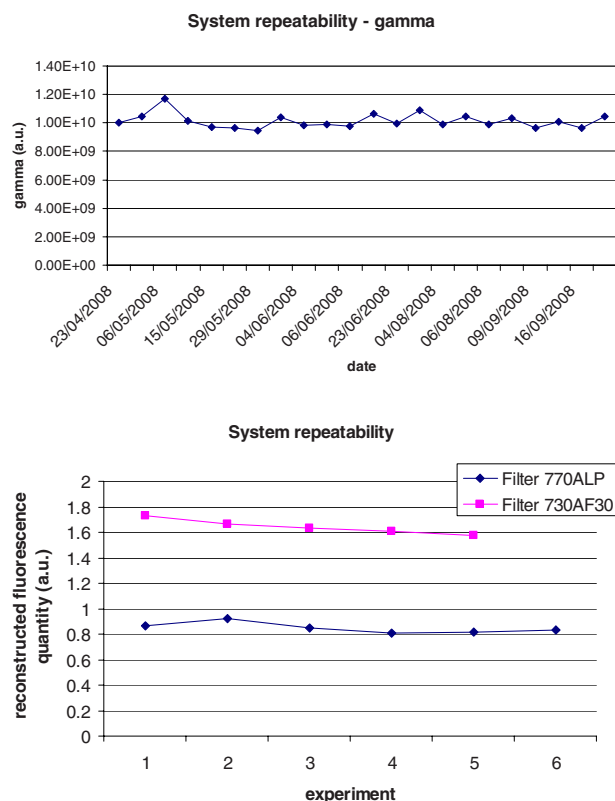


Fig. 7 Top: Repeatability of the system showing a good stability of the γ parameter over a 5-month period. Bottom: Repeatability of the experiments. The fluorescence quantity is measured in the overall reconstructed volume and is stable with the experiments.

scans the animal in order to get its surface, as described earlier. Then, the animal is scanned by the near-infrared (NIR) laser. Typically, the excitation sources describe a regular 11 by 11.2 mm-spaced grid (2 cm \times 2 cm field of view) drawn in red in Fig. 8. For each source position, the CCD camera focused at the mean thickness of a mouse (i.e., 15 mm) first records the transmitted (excitation) images. Then a filter is inserted, and the fluorescence (emission) images are recorded.

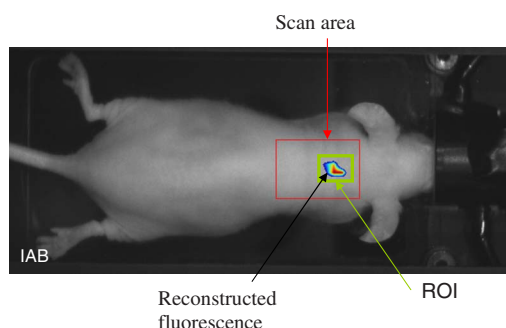


Fig. 8 Mouse experiment: A capillary tube containing Alexa 700 is inserted in the trachea of a mouse. The mouse is maintained between two glass plates with a thickness of 15 mm. The reconstructed fluorescence is presented in superimposition over the mouse photograph. (Color online only.)

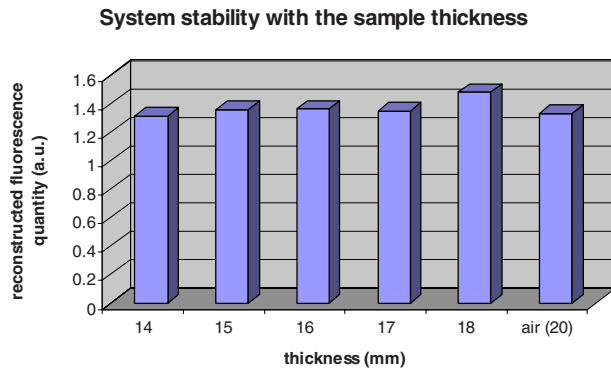


Fig. 9 Results showing the good reproducibility of the experiment and the stability of the tomograph according to the animal thickness.

3.5 Reproducibility with Thickness

We conducted a set of free-space *in vivo* experiments on female Swiss nude mice in order to compare the results to those obtained with the previous configuration of the system when the mice were maintained between two glass plates.

In the “between-plates” configuration, the mouse lies on its ventral side and is maintained between the two glass plates of the heating support. By varying the compression of a mouse, we acquired tomographic measurements for the mouse thickness ranging from 14 to 18 mm. Thereafter, we performed a free-space experiment where the uncompressed mouse (20 mm thickness) lay in its physiological position. The mouse has a capillary tube—filled with $0.4 \mu\text{l}$ of a solution of Intralipid and a quantity of 3.6 pmol Alexa 700—inserted in its trachea. We choose to inspect the lung area by reference to the previous study presented in Ref. 4.

The between-plates experiments are reconstructed using the previous method, which takes into account the animal area in contact with the upper glass plate given by an illumination of the animal by the lateral sides. As in this experiment, we reconstruct a capillary that is in a delimited area, and during reconstruction, we use only 10 by 8 positions (that is, 80 sources), and we consider only the detectors of the camera for which the projection is in the area in contact with the animal or in the neighboring extrapolated area. The total number of detectors (binned pixels of $500 \mu\text{m}$) of this reduced scan area is 1665. The percentage of detectors used when we use the compression plate varies from 45 to 55% of total detectors. The free-space experiment uses the surface information in order to exploit data coming from the whole animal, and we use 90% of the detectors. (100% represents all the detectors that cover the scanned area.)

Figure 8 presents the projection of the reconstructed fluorescence volume over the black-and-white photograph of the mouse for the 15-mm-thickness between-plates experiment. We measure the reconstructed signal in a $5 \text{ mm} \times 3 \text{ mm}$ region of interest drawn in light green centered over the capillary tube and compare the values from one experiment to the other, as shown on Fig. 9. This measurement done on a 2-D projection represents the sum of the fluorescence found in a $5 \times 3 \times 15 \text{ mm}^3$ volume. The total reconstructed fluorescence is stable within 3% (deviation from “between plates” average)

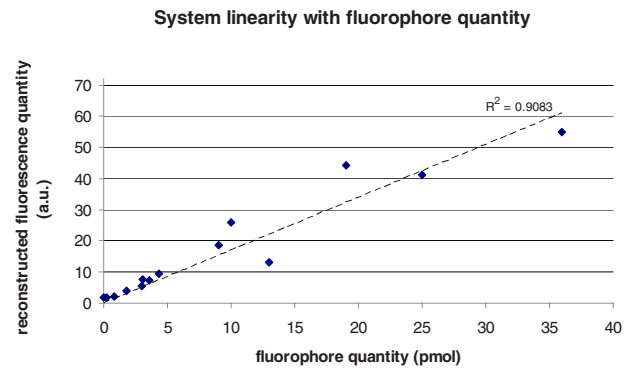


Fig. 10 Results showing linearity of the tomograph according to the quantity of fluorophore inside the capillary tube inserted in the mouse.

and, the free-space and between-plates results are in accordance. This experiment validates the free-space functionality.

3.6 Linearity with Fluorophore Quantity

In order to validate the quantification done on experiments conducted in the free-space configuration, several similar experiments have been repeated using different quantity of fluorophore inside the capillary tube. We use a range of quantity from 0.2 pmol to 20 pmol of Alexa 700 diluted into a specific marker used for pulmonary cancerous inspection Angiolone–Alexa 700 (FluoOptics, Grenoble, France). The capillary tube is inserted in the mouse trachea, and the mouse lung area is scanned with the mouse placed in its physiological position in the free-space tomograph configuration.

We measure the reconstructed signal in a $18 \text{ mm} \times 18 \text{ mm}$ region of interest centered over the capillary tube. This measurement done on a 2-D projection of the z slices of the reconstructed volume represents the sum of the fluorescence found in an $18 \times 18 \times 15 \text{ mm}^3$ volume. The scale is in arbitrary units (a.u.) because the tomography gives relative values, not absolute values. In order to give absolute values, a calibration with etalon phantoms has to be done.

The curve presented in Fig. 10 shows the good linearity of the system with the fluorophore quantity inside the capillary tube (coefficient of determination R^2 is 0.9). The deviation from linearity ranges from 3.3% to 40%, except for two values: 13 pmol and 0.26 pmol, for which the deviation is 67% and 75%, respectively. For higher fluorophore concentrations, another phenomenon of self-absorption of the fluorophore occurs that prevent a portion of the emitted light reaching the detectors.

3.7 Longitudinal Study on a Diseased Mouse

Last, we conducted an *in vivo* experiment on a diseased mouse in order to follow up the growth of mammary murine tumors and to validate the free-space configuration in its use for *in vivo* disease follow-up.

The mouse is imaged at 10, 12, and 14 days after the primary mammary adenocarcinoma cells implantation; 10^6 TSA/pc (Trichostatin A) cells in $100 \mu\text{l}$ phosphate-buffered saline (PBS) solution. A delay of two days between two successive measurements has been chosen because it is the time required for the animal to totally eliminate the fluorescent

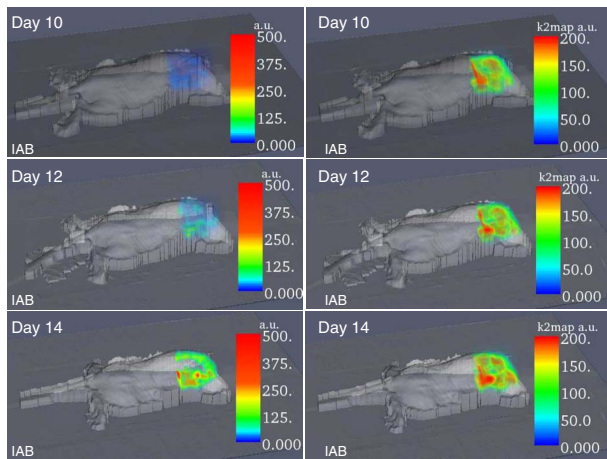


Fig. 11 Left: 3-D view of the reconstructed fluorescence quantity superimposed on the white-light image for a diseased mouse at day 10 (top), day 12 (center), and day 14 (bottom) after the tumor implantation. The increase of the fluorescence follows the development of the disease. Right: 3-D view of the attenuation map k superimposed on the white-light image for a diseased mouse at day 10 (top), day 12 (center), and day 14 (bottom) after the tumor implantation. A slight modification of the map can be seen.

probe. The tumor cells are injected by the tail vein; the first organs encountered are the lungs, and the cells stay fixed there.

The mouse lies on its ventral side and is simply placed on the heating support in its physiological position in the free-space tomography configuration. The mouse is injected with a specific marker Angiolone–Alexa 700 (Fluooptics, Grenoble, France; 200 μ l). It has been shown that this probe targets the $\alpha v \beta 3$ integrin, which is overexpressed in tumors.^{17,18} Three hours later, the mouse is anesthetized, and the lung area is scanned with infrared light describing an 11 by 11.2 mm–spaced grid.

The superimposition of the reconstructed volumes of the mouse at days 10, 12, and 14 and of the scanned surface of the animal onto the white-light images [Fig. 11 (left)] shows the progression of the lung cancer invasion in the animal. The three reconstructed volumes are presented using the same colormap to allow comparison. The right part of Fig. 11 shows the attenuation map k . The k map variation with the evolution of the disease is smoother than the fluorescence variation. The slight evolution can be explained by the invasion of the tumor tissues in the lungs. This study gives similar results to the study previously carried out with the mouse maintained between plates and described in Ref. 4, and thus validates the use of the tomography in the free-space configuration for disease follow-up.

4 Conclusion and Discussion

The results detailed in this paper present the evaluation of the improvements done on our preclinical tomograph. The coherence of the results with the system maintaining mice between plates has been assessed. Reproducibility and linearity of the measurements has been established, and *in vivo* results using capillary tubes are encouraging and validate the performance of our system and its dedicated reconstruction methodology

for preclinical biological studies. This opens the way for using this system in free-space routine experiments.

The free-space experiment done on a mouse bearing mammary murine tumors shows similar results as in a between-plates previous study and, due to the free-space capability, greatly facilitates the animal manipulation. We also showed the feasibility of studies using two different fluorophores simultaneously in the same *in vitro* experiment. These two results are promising and should be considered for *in vivo* experiments on mice for which two types of cells can simultaneously be marked by two fluorophores and examined in their physiological position.

Acknowledgments

The authors would like to thank Mélanie Guidetti of Institut Albert Bonniot, who took care of the animals and prepared them for the experiments presented in this paper. This work has been partly funded by CLARA, the IPA project, the Emil DiMI Network of Excellence, and the RTB.

References

1. V. Ntziachristos, E. A. Schellenberger, J. Ripoll, D. Yessayan, E. Graves, A. Bogdanov, L. Josephson, and R. Weissleder, "Visualization of antitumor treatment by means of fluorescence molecular tomography with an annexin V-Cy5.5 conjugate," *PNAS* **101**(33), 12294–12299 (2004).
2. H. A. Shih, S. D. Windsor, R. Weissleder, and V. Ntziachristos, "In vivo characterization of Her-2/neu carcinogenesis in mice using fluorescence molecular tomography," Paper TuC1 in Biomedical Optics 2006 Technical Digest, Optical Society of America, Washington, DC, p. TuC1 (2006).
3. R. B. Schulz, J. Ripoll, and V. Ntziachristos, "Experimental fluorescence tomography of tissues with noncontact measurements," *IEEE Trans. Med. Imaging* **23**(4), 492–500 (2004).
4. A. Koenig, L. Herve, V. Jossierand, M. Berger, J. Boutet, A. DaSilva, J. M. Dinten, P. Peltie, J. L. Coll, and P. Rizo, "In vivo mice lungs tumors follow-up with fDOT," *J. Biomed. Opt.* **13**(1), 011008 (2008).
5. R. Schulz, J. Peter, and W. Semmler, "A non-contact fluorescence tomography system for small animal imaging," Paper TuG8 in Biomedical Optics Technical Digest, Optical Society of America, Washington, DC (2006).
6. T. Troy, D. G. Stearns, D. N. Nilson, and B. W. Rice, "Development of a 3D optical imaging system for in vivo detection of bioluminescence," Paper TuD4 in Biomedical Topical Meeting, Optical Society of America, Washington, DC, p. TuG8 (2002).
7. L. Hervé, A. Koenig, A. Da Silva, M. Berger, J. Boutet, J. M. Dinten, P. Peltié, and P. Rizo, "Noncontact fluorescence diffuse optical tomography of heterogeneous media," *Appl. Opt.* **46**, 4896–4906 (2007).
8. R. Aronson, "Boundary conditions for diffusion of light," *J. Opt. Soc. Am. A* **12**, 2532–2539 (1995).
9. R. B. Schulz, J. Ripoll, and V. Ntziachristos, "Noncontact optical tomography of turbid media," *Opt. Lett.* **28**(18), 1701–1703 (2003).
10. A. Koenig, L. Hervé, J. Boutet, M. Berger, J. M. Dinten, A. Da Silva, P. Peltié, and P. Rizo, "Fluorescence diffuse optical tomographic system for arbitrary shaped small animals," in 5th IEEE International Symposium on Biomedical imaging: From Nano to Macro, ISBI, pp. 1593–1596 (2008).
11. S. R. Arridge, "Optical tomography in medical imaging," *Inverse Probl.* **1**, R41–R93 (1999).
12. T. Takamura, N. Takahashi, T. Ishigami, T. Sugano, T. Ishikawa, K. Uchino, K. Kimura, T. Inoue, and S. Umemura, "Combining chronic kidney disease with 201thallium/123iodine beta methylodophenyl pentadecanoic acid dual myocardial single-photon emission computed tomography findings is useful for the evaluation of cardiac event risk," *Nucl. Med. Commun.* **30**(1), 54–61 (2009).
13. M. Longmire, A. J. Gunn, N. Y. Morgan, P. D. Smith, T. J. Pohida, Y. Koyama, H. Kobayashi, and P. L. Choyke, "Real-time fluorescence-enhanced imaging as an aid to surgery in ovarian cancer," *IEEE J. Sel. Top. Quantum Electron.* **13**(6), 1602–1609 (2007).

14. N. Kosaka, M. Ogawa, M. R. Longmire, P. L. Choyke, and H. Kobayashi, "Multi-targeted multi-color *in vivo* optical imaging in a model of disseminated peritoneal ovarian cancer," *J. Biomed. Opt.* **14**(1), 014023 (2009).
15. J.-M. Dinten, P. Peltié, A. da Silva, J. Boutet, A. Koenig, L. Hervé, M. Berger, A. Laidevant, and P. Rizo, "Performances of different reflectance and diffuse optical tomographic approaches in fluorescence molecular imaging of small animals," *Proc. SPIE* **6142**, 614215 (2006).
16. U. Brackmann, *Lambdachrome Laser Dyes*, 3rd ed., Lambda Physik GmbH, Göttingen, Germany (2000).
17. D. Boturyn, J. L. Coll, E. Garanger, M. C. Favrot, and P. Dumy, "Template assembled cyclopeptides as multimeric system for integrin targeting and endocytosis," *J. Am. Chem. Soc.* **126**(18), 5730–5739 (2004).
18. E. Garanger, D. Boturyn, Z. Jin, P. Dumy, M. C. Favrot, and J. L. Coll, "New multifunctional molecular conjugate vector for targeting, imaging, and therapy of tumors," *Mol. Ther.* **12**(6), 1168–1175 (2005).